Volume 4, Issue 3, 2018

Journal of Biomedical Photonics & Engineering

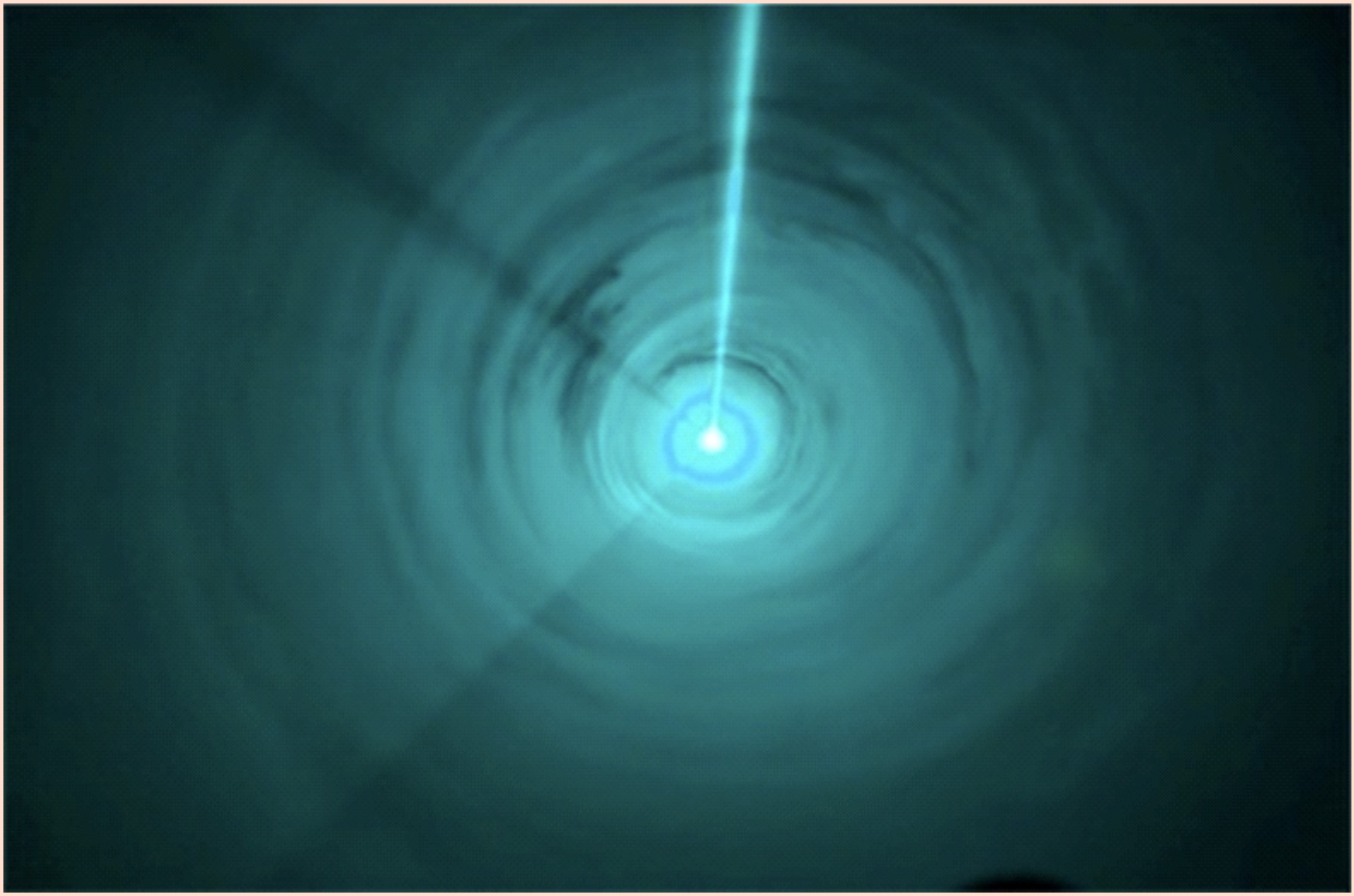

 doi: 10.18287/JBPE18.04.030001

Journal of Biomedical Photonics & Engineering

by Samara National Research University

Volume 4, Issue 3 (September 2018)

Editorial Board

Postal address:
39B Lukacheva st., room #301
Samara 443086, Russian Federation

Contents

Articles

Peculiarities of soft biological tissue perforation induced by near infrared laser radiation with optic fiber delivery

Alexandr K. Dmitriev, Alexey N. Konovalov*, Vladimir N. Kortunov, and Valerii A. Ulyanov
Institute of Photonic Technologies, Federal Scientific Research Centre 'Crystallography and Photonics' of the Russian Academy of Sciences, 2 Pionerskaya Str., Moscow, Troitsk 108840, Russia

* **e-mail:** ank27.ift@mail.ru

Abstract. The authors studied the process of perforation of soft biological tissue by continuous near infrared lasers (0.98 μm, 1.56 μm and 1.94 μm) with optic fiber delivery. Fiber drag force (FDF) during perforation of soft biological tissue was studied. Specific characteristics of laser radiation heat impact on the tissues surrounding the laser channel were examined. Three perforation modes were observed: mechanical perforation mode, intense evaporation and tissue destruction mode, "free" perforation mode. In the first mode, FDF is almost identical to FDF in the absence of radiation. In the second mode, FDF is significantly lower than FDF during laser radiation power of P = 0. In the third perforation mode, the formed channel becomes wider than the fiber diameter due to intense tissue evaporation and burning, and FDF is close to or below the sensitivity limit of the force sensor. The effect of burnt tissue deposit at the fiber tip on the laser perforation process was studied.

Keywords: fiber laser; laser perforation; biological tissue; regeneration.

Paper #3297 received 2 Aug 2018; revised manuscript received 25 Aug 2018; accepted for publication 25 Aug 2018; published online 12 Sep 2018. doi: 10.18287/JBPE18.04.030301.

References

1. I. I. Berishvili, Transmyocardial Laser Revascularisation, GEOS, Moscow, Russia (2016) [in Russian]. ISBN 978-5-89118-703-0.
2. D. I. Alyokhin, A. A. Fokin, "Prospects of using high-intensity laser radiation for the treatment of chronical ischemia of extremities," Patologiya krovoobrashcheniya i kardiokhirurgiya 2, 88-92 (2005) [in Russian].
3. S. V. Kapralov, I. A. Melnikova, U. G. Shapkin, and V. V. Alipov, "Experimental modeling of laser fenestration of the liver," Bjulleten' meditsinskih Internet-konferentsij 11(2), (2011) [in Russian].
4. I. A. Shved, T. E. Vladimirskaya, A. V. Vorobey, O. P. Shorez, S. V. Alexandrov, and A. C. Shuleiko, "Liver tissue regeneration after laser coagulation," Zdravookhraneniye (Belarus) 3, 4-8 (2014) [in Russian].
5. L. V. Astahova, E. N. Ignat'eva, E. S. Golovneva, R. U. Giniatullin, and T. G. Kravchenko, "Morphofunctional changes in the foci of laser destruction of the liver, kidney, spleen (experimental study)," Laser medicine 20(1), 50-54 (2016) [in Russian].
6. V. Tuchin, Tissue optics. Light scattering methods and instruments for medical diagnosis, SPIE press, Belingham, Washington, USA (2012).
7. L. Kou, D. Labrie, and P. Chylek, "Refractive indices of water and ice in the 0.65 – 2.5 μm spectral range," Applied Optics 32(19), 3531-3540 (1993).
8. B. I. Sandler, L. N. Suljandziga, V. M. Chudnovskij, V. I. Jusupov, O. V. Kosareva, and V. S. Timoshenko, Perspectives of treatment of discogenic compression forms of lumbosacral radiculitis with the help of puncture non-endoscopic laser operations, Dal'nauka, Vladivostok, Russia (2004) [in Russian]. ISBN: 5-8044-0443-1.
9. V. I. Yusupov, V. M. Chudnovskii, and V. N. Bagratashvili, "Laser-induced hydrodynamics in water-saturated biotissues: 2. Effect on delivery fiber," Laser Physics 21(7), 1230-1234 (2011).

10. V. V. Elagin, M. A. Shahova, M. M. Karabut, D. S. Kuznetsova, V. I. Bredihin, N. N. Prodanets, L. B. Snopova, O. S. Baskina, A. V. Shahov, and V. A. Kamenskij, "Evaluation of the cutting properties of a laser scalpel equipped with a highly absorbing coating of an optical fiber," Sovremennye tehnologii v meditsine 7(3), 56-60 (2015) [in Russian].
11. H.-P. Berlien, G. J. Müller (eds.), Applied Laser Medicine, Springer-Verlag, Berlin (2003).
12. J. T. Walsh, T. F. Deutsch, "Pulsed CO_2 laser ablation of tissue: effect of mechanical properties," IEEE Transactions on Biomedical Engineering 36(12), 1195-1200 (1989).
13. V. A. Berezovskii, N. N. Kolotilov (eds.), Biophysical Characteristics of Human Tissues, Naukova dumka, Kiev, USSR (1990) [in Russian].
14. V. L. Utkin, Biomechanics of physical exercises, Prosveschenie, Moscow (1989) [in Russian].

1 Introduction

Use of high intensity laser radiation for stimulation of tissue regeneration in vital human organs through creation of deep laser channels in biological tissues is one of the promising medical trends. In particular, this approach to coronary heart disease treatment allowed to develop an efficient method for laser myocardium revascularisation, ensuring its stimulation and long-term angiogenesis [1]. Laser perforation is also becoming a popular method of stimulating regeneration processes in other soft biological tissues. In particular, positive effect of ischemic lower limb laser revascularization with 0.98 and 1.06 μm radiation delivered by optic fiber is now known. The positive effect lasts for up to 6 months with further deterioration of the patients' clinical status [2]. Laser regeneration of cirrhotic rat liver has been performed with semiconductor laser radiation (wavelength 1.06 μm): it resulted in liver regeneration with formation of microcapillaries and bile ducts in the area of laser perforation with optic fiber [3]. Active work is underway to find optimal conditions for laser regeneration of this vital organ in humans [4, 5].

Two methods have become popular for laser formation of deep channels: 1) focused radiation in single pulse mode; 2) use of optic fiber, where perforation is carried out by moving the optic fiber with set speed into the depth of biological tissue. Obviously, these are two different approaches resulting in different physical effects in the area of perforation, and therefore different tissue and body responses to such impacts are to be expected.

If tissue is perforated by focused radiation, the channel is formed through tissue evaporation, while optic fiber perforation may include a combination of actions: mechanical impact of the optic fiber upon the tissue and its evaporation by laser radiation. Near infrared laser radiation sources with wavelength of 0.9 μm to 2 μm are most often used for optic fiber perforation of biological tissues. In this spectral range, the absorption coefficient of soft water-containing tissues (water content 70% and more) can vary considerably [6], since water in this range has absorption bands. For example, for the widely used wavelengths of laser sources, the absorption coefficient of water differs by orders of magnitude: it is 0.5 cm^{-1} for 0.98 μm, 10 cm^{-1} for 1.56 μm and 135 cm^{-1} for 1.94 μm [7]. Consequentially, the process of biological tissue perforation may go differently within this wave range, both in conditions of spatial and subsurface absorption of laser radiation power by the biological tissue. Another specific characteristic of contact perforation of biological tissue with optic fiber is the changing conditions of radiation heat impact, both due to the effect of burnt tissue deposit at the fiber tip, naturally occurring directly in the process of biological tissue perforation, and as a result of special absorbing coating created at the fiber tip or fiber tip blackening [8, 9, 10].

Thus, laser perforation of biological tissue performed through optic fiber may result in different physical phenomena, depending on the impact conditions. However, physical aspects and specific characteristics of deep channel formation in biological tissues induced by optic fiber have not been sufficiently described in scientific literature.

The purpose of this research is the comparative study of biological tissue perforation by near infrared laser radiation with optic fiber delivery in various impact modes.

2 Materials and methods

CW-pumped lasers were used as sources of laser radiation: 1 – semiconductor laser with power up to 10 W and 0.98 μm wavelength (Ltd Company "RIK"); 2 – fiber optic multimode laser with 1.56 μm wavelength and power up to 10 W (NPO "IRE-Polus"); 3 – fiber optic multimode laser with 1.94 μm wavelength and power up to 15 W (NPO "IRE-Polus").

Multimode fiber with diameter of 600 ± 30 μm was used for radiation delivery. Output power applied to the biological tissue was measured by FieldMaster (Coherent) power meter. A655sc (FLIR) thermal camera was used to measure the temperature of the fiber tip; it was equipped with an extra lens to amplify and obtain an image with resolution of 50 μm per pixel.

A mechanic sensor system (MSS) (Fig. 1) was created in order to study the process of biological tissue perforation by near infrared laser radiation with optic fiber delivery, which registered biological tissue drag force during its perforation with optic fiber.

This system included mechanic sensor unit 4 to convert fiber drag force to voltage using a force sensor and analog-to-digital converter 6 to record and analyze

the signal on a PC 8. The sensitivity of this system was (69 ± 1) mV/N.

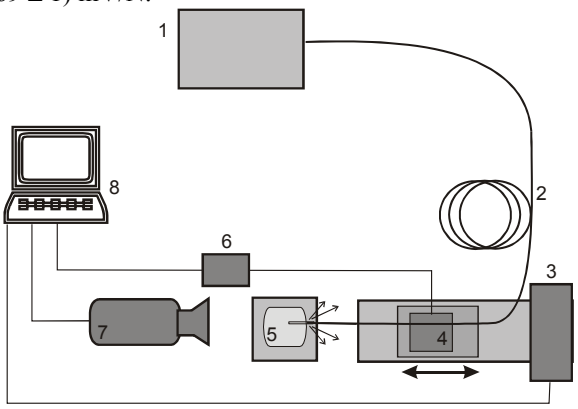

Fig. 1 Schematic diagram of the experimental setup. 1 – fiber laser; 2 – multimode fiber; 3 – motorized linear translator; 4 – mechanic sensor system; 5 – biotissue; 6 – analog-to-digital converter; 7 – thermal camera; 8 – PC.

15×10×5 mm samples of fresh pig muscle tissue *in vitro* were used as the target. The tissue was obtained and used within 48 h post mortem. The samples were stored at 0-4 °C and at controlled humidity. The samples were placed on a stationary platform. The samples were perforated by moving the fiber into the depth of the tissue by a motorized linear translator 3 (Fig. 1) with set speed. The biological tissue samples were pierced. After perforation the samples were frozen in order to fix the form of the laser channel. After this, longitudinal and cross sections were made in the channel area, and the channel diameter and the size of the thermal damage area (TDA) in the tissue surrounding the channel were measured. Tissue TDA included two zones: carbonization zone and tissue coagulation zone. These zones were determined on change of tissue color after perforation. Carbonization zone adjacent to laser channel wall have black-and-brown color. Coagulation zone have whitish color. Such tissue color changes at temperatures above 60 °C – this is caused by protein denaturation [10]. TDA size was determined as the distance from the laser channel wall to the border of the whitish tissue. Channel geometry and the size of the thermal damage area (TDA) of the biological tissue were determined using an MBS-10 stereoscopic microscope with 100x magnification.

3 Results and Discussion

Fig. 2 shows typical time sweeps of the MSS signal during muscle tissue perforation. The data are given for a laser with 0.98 μm wavelength and 0.5 mm/s fiber movement speed. Three patterns may be distinguished on the tissue fiber drag force (FDF) time curve during perforation: 1) continuous increase of the drag force; 2) signal fluctuation in reference to the average level; 3) rapid decrease of the signal.

This FDF behavior may be explained as follows. The registered drag force of the tissue during its perforation by the fiber is made up of two components: drag force at the fiber tip and friction at the fiber's lateral surface during its movement inside the channel in the tissue. During the initial period, after the fiber touches the tissue surface, the signal starts to gradually increase due to tissue contraction. The signal continues to increase until FDF remains insufficient to make a hole in the tissue. In the extreme case, when laser radiation power is zero, the signal continues to increase until the force exceeds tensile strength of biotissue. The second pattern in the MSS signal is due to the fact that the pressure force at the fiber tip is sufficient to tear the tissue and start forming a hole. There are significant FDF fluctuations in this pattern. This is explained by intermittent tissue contraction, followed by a power drop during the next local tissue tear at the fiber tip. The fluctuations may also be caused by the non-steady process of tissue evaporation near the fiber tip. Herewith, intensive ejection of tissue destruction products from the entrance hole was occasionally observed in the form of smoke and vapor (due to tissue water evaporation).

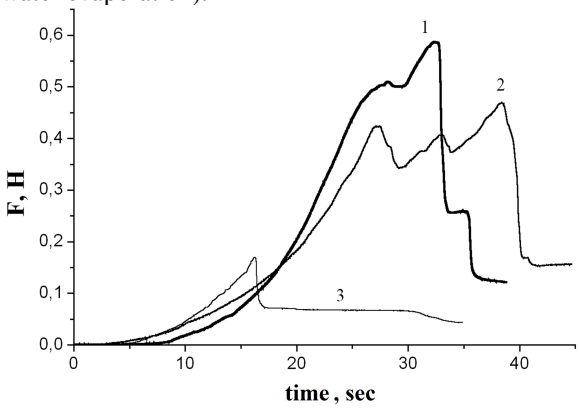

Fig. 2 FDF as a function of time in the perforation of muscle tissue by laser fiber at different radiation powers (1 – 1.7 W; 2 – 2.3 W; 3 – 4.5 W). V = 0.5 mm/s, λ = 0.98 μm.

The third FDF pattern is explained the formation of a through hole in the tissue. In this case, there is no more tissue pressure on the fiber tip, and the registered force is conditioned by the friction force at the fiber's lateral surface.

We have studied FDF with various laser radiation power and various speed of fiber movement into the depth of the tissue. Each piercing of the tissue was characterized by the maximum force registered by MSS. Fig. 3 shows the variation of the maximum FDF with respect to laser radiation power with perforation speed of 0.5 mm/s for three wavelengths: 0.98 μm, 1.56 μm and 1.94 μm. Before each new perforation the fiber tip was split off (perforation with a "clean" fiber tip), and output radiation power was measured.

Fig. 3 shows that with 0.98 μm wavelength there is a power range of 0-2.5 W, where FDF almost does not change and coincides with the drag force during fiber perforation of the biological tissue in the absence of radiation (P = 0 W). FDF rapidly decreases in radiation

power range of 2.5-3.5 W. With a wavelength of 1.94 μm there is no range where FDF does not change. Herewith, when the power is 2 W, FDF is approximately ten times lower than in the absence of radiation. With higher radiation power (over 2.5 W for λ = 1.94 μm and over 6 W for λ = 0.98 μm), FDF decreases below the limit of detection (0.002 N) of the mechanic sensor system.

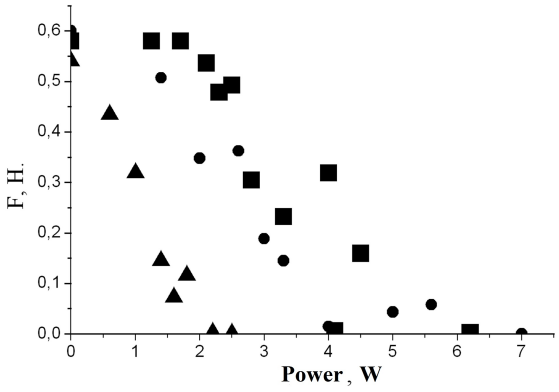

Fig. 3 Dependence of FDF on the power of laser radiation at different wavelengths (■ – 0.98 μm; ● – 1.56 μm; ▲ – 1.94 μm). V = 0.5 mm/s.

This FDF behavior depending on the power of the laser radiation is conditioned by the forming of various thermal physical processes near the fiber tip. In the absence of radiation, the channel is formed due to mechanical tear of the tissue. If the power is increased, additional microexplosions may form near the fiber tip as bubbles appear, when water contained in the tissue begins to boil. As a result, less force is required to tear the tissue during fiber movement. If radiation power is further increased, the processes of intensive evaporation and tissue burning come into effect. In this mode, a channel is formed near the fiber tip due to intensive evaporation and tissue destruction caused by radiation. In these conditions, FDF is almost zero because the fiber tip has no contact with dense tissue. The drag force conditioned by friction of channel lateral walls may also significantly decrease in this mode, as the channel widens when tissue destruction products are discharged. As the tissue absorption coefficient is more than 100 times higher for a wavelength of 1.94 μm than for a wavelength of 0.98 μm [6], the thresholds for formation of micro tears and intensive evaporation are significantly lower for a wavelength of 1.94 μm.

FDF has such a broad range of fluctuations for two reasons. First, muscle tissue is not homogenous. *Inter alia*, the muscle tissue samples used may have blood vessels, fascia, fat tissue inclusions. The strength characteristics of these tissue components differ significantly: muscle tissue – 0.1-0.3 N/mm^2, blood vessels – 0.4-2 N/mm^2, skin – 2-36 N/mm^2, fascia – (12-14 N/mm^2) [12-14]. Thus, when the fiber moves into the depth of the tissue, the FDF signal may fluctuate significantly, depending on which part of the perforated tissue it passes through. The second reason for the wide range of FDF figures is the non-steady nature of the perforation process, caused by non-steady heating, evaporation and the ejection of vapor and gas from the channel.

In the absence of radiation, the perforation process directly depends on the strength characteristics of the muscle tissue. In this case, FDF is 0.55 ± 0.05 N. With fiber diameter 600 μm it corresponds to the pressure of 1.9 ± 0.2 N/mm^2. This value is higher than the muscle tissue strength limit by an order of magnitude and approximately corresponds by the order of magnitude to the strength limit of vessel and skin tissue. We believe that the significant difference between FDF signal and muscle strength limit is explained by the fact that FDF is a pressure force, while the data related to strength limits of tissue components were determined by the force directed at tissue tear. When fiber exerts pressure on the tissue, there is a local redistribution of forces within the tissue. Force components directed at tissue tear also appear in this case, but they are naturally lower than the direct fiber pressure force.

Fig. 4 shows how FDF depends on fiber movement speed during perforation of the sample with radiation of 4 W and wavelength of 1.56 μm. This dependence also confirms conclusions regarding the different impact modes during perforation by laser fiber. When the fiber moves at low speeds, the tissue is considerably overheated, reaching high temperatures. This causes a vapor and gas channel to form near the fiber tip, and tissue destruction products are ejected along the lateral walls. In this case, the fiber almost does not touch the tissue, resulting in a quite low FDF. If the fiber movement speed increases, the tissue does not have the time to heat up to high temperatures, therefore no vapor and gas channel is formed and, as a result, the fiber mechanically touches the tissue, and FDF increases.

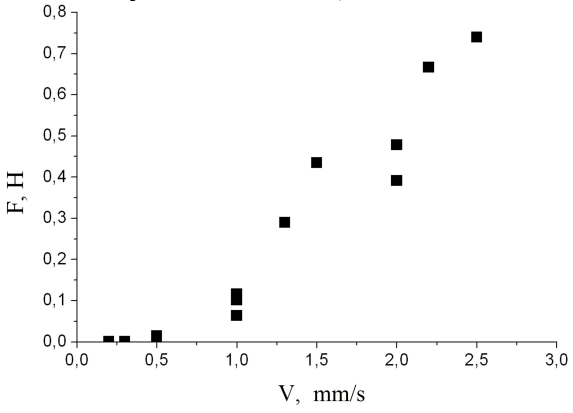

Fig. 4 Dependence of FDF on the speed of perforation of muscle tissue by laser fiber. P = 4 W, λ = 1.56 μm.

It is known that during laser perforation of the biological tissue with optic fiber, burnt tissue is deposited on the fiber tip as a result of tissue carbonization. This may lead both to decrease of radiation output from the fiber and to the fiber tip reaching high temperatures [8, 9]. We have measured radiation power output, fiber tip heating temperature and FDF during 5 and more consecutive piercings of

1.5 cm-thick biological tissue. In these experiments, the fiber tip was split off before the first perforation, and all the following perforations were done with non-split fiber. Power output and fiber tip temperature in the air (before touching the biological tissue) were measured before each consecutive perforation. It was discovered that in the process of perforation, the carbonized burnt tissue deposit at the fiber tip insignificantly decreases output radiation power (by 5-20 %), while fiber tip temperature may vary significantly within the range from 25-30 °C (in the absence of burnt tissue deposit at the fiber tip) to hundreds and even a thousand degrees Celsius. It was established that on average the significant burnt tissue deposit, manifesting itself in the high temperature of the fiber tip (over 100 °C), occurs after the third or fourth piercing of the 1.5 cm-thick biological tissue. With such burn tissue deposit, FDF significantly decreases, in particular below the sensitivity limit of MSS sensor. Fig. 5 shows the variation of FDF with respect to time for the 2nd, 3rd and 4th perforation and the corresponding fiber tip temperature.

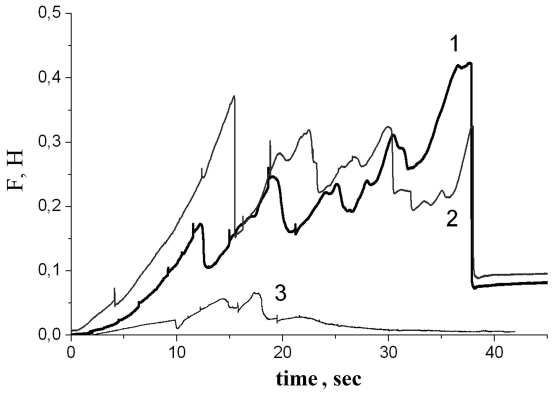

Fig. 5 FDF as a function of time in the perforation of muscle tissue by laser fiber. 1 – perforation №2, P = 2.6 W, T = 85 °C; 2 – perforation №3, P = 2.9 W, T = 85 °C; 3 – perforation №4, P = 3.0 W, T = 350 °C. V = 0.5 mm/s, λ = 1.56 μm.

When biological tissue is perforated, concentric layers of thermally damaged tissue are formed around the laser channel, where carbonization and coagulation zones may be singled out (Fig. 6b). The boundary of the coagulation zone corresponds to the visible borders of the tissue of whitish color [10]. The tissue changes its color due to protein denaturation, occurring at temperatures above 60 °C (60-70 °C with heating time of 1-1000 ms). More significant heating of the tissue up to the temperature of 300-400°C leads to its carbonization. The size of the carbonization area may also be determined visually (using a regular microscope), as a dark brown tissue layer which borders with the ablative zone (Fig. 6). The borders of coagulation zone determine the size of the thermally damaged area of the tissue.

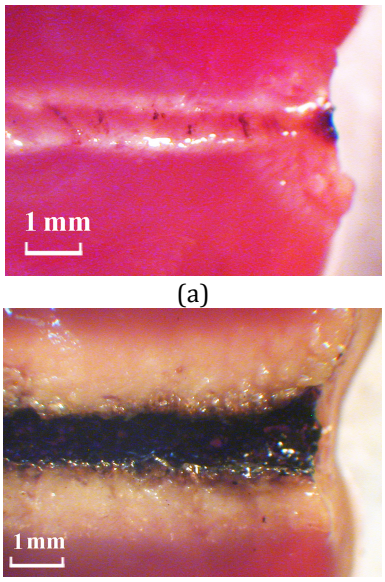

Fig. 6 Images of channels in biological tissues formed by a laser fiber. V = 0.5 mm/s, λ = 0.98 μm. (a) P = 3 W; (b) P = 8 W.

Histograms on Figs. 7 and 8 show the variation of TDA width and laser channel (LC) diameter with respect to wavelength and laser radiation power. Sample perforation speed was maintained at a constant rate of 0.5 mm/s. The laser channel diameter, seen through the microscope (Fig. 7) is in some cases (with low laser radiation power and wavelengthof 0.98 μm and 1.56 μm) smaller than the diameter of the laser fiber core, which is 600 μm. This is explained by the elasticity of the channel walls which sustained no significant thermal damage. In this case, the channel is formed due to tissue tear; later, the channel contracts naturally. Larger FDF corresponds to this power range (see Fig. 3). Increased radiation power leads to enlargement of the channel due to destruction and evaporation of the biological tissue along the fiber movement route (Fig. 7); simultaneously, drag force decreases (Fig. 3). The fiber moves freely in the tissue when the channel diameter increases to the size of the fiber core (600 μm) and more, with laser radiation power of 5-6 W (Fig. 3).

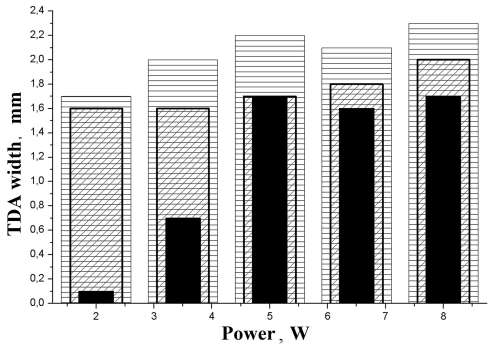

Fig. 7 Dependence of the TDA width on the wavelength and power of laser radiation. (■ – 0.98 m, ▒ – 1.56 m, //// – 1.94 m).

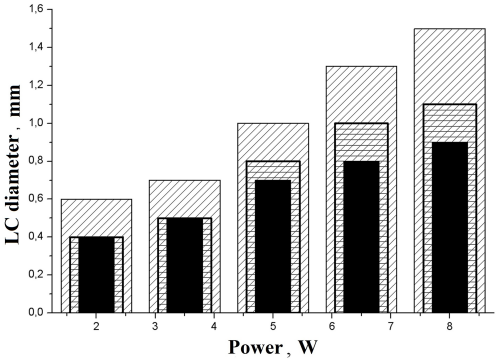

Fig. 8 Dependence of laser channel diameter on the wavelength and power of laser radiation. (■ – 0.98 m, ▒ – 1.56 m, //// – 1.94 m).

4 Conclusions

The process of perforation of muscle tissue *in vitro* using near infrared laser radiation with optic fiber delivery was studied. The study of the drag force during movement of the fiber into the depth of the tissue makes it possible to distinguish three modes of tissue perforation:

1. Mechanical perforation mode: FDF almost does not depend on the laser radiation power and coincides with the drag force during piercing of the biological tissue with the fiber in the absence of radiation (P = 0 W). This mode was observed for 0.98 μm wavelength in the power range of 0-2.5 W with constant perforation speed of 0.5 mm/s.

2. Intense evaporation and tissue destruction mode: FDF value drops as laser radiation power increases. This mode is applicable for all used laser sources. Its limits are primarily determined by laser radiation absorption efficiency of the biological tissue and fiber movement speed.

3. "Free" perforation mode: FDF is almost zero, as the fiber tip has no contact with dense tissue due to burning and evaporation of the biological tissue at the fiber tip and the increased diameter of the laser channel. "Free" perforation mode is applicable for 1.94 μm wavelength with power above 2 W and for wavelengths of 1.56 and 0.98 μm with power above 4 W.

It has been demonstrated that the drag force during muscle tissue perforation increases, if the speed of fiber movement into the depth of the tissue increases. When the fiber movement speed is low, the tissue becomes significantly overheated, and the third perforation mode is realized with FDF almost at zero value. If the speed of fiber movement into the depth of the tissue increases, the second mode gradually comes into effect with a gradual FDF increase.

Drag force measurement allows to evaluate the impact of carbonized burnt tissue deposit at the fiber tip on the perforation process. It has been established that on average burnt tissue deposit causing the fiber tip to heat up above 100 °C occurs after the third or fourth piercing of the biological tissue. With such burnt tissue deposit, FDF value drops to the sensitivity limit of the MSS sensor.

Channels formed during laser perforation of pig muscle tissue were examined with microscopes. Dependence of the thermal damage area and channel diameter on laser radiation power with perforation speed of 0.5 mm/s was studied. Microscopic research of the biological tissue in the area of formed laser channels confirms the conclusion that there exist 3 various impact modes.

Disclosures

All authors declare that there is no conflict of interests in this paper.

Acknowledgment

This research was supported by grant No. 15-29-04816 of the Russian Foundation for Basic Research and by the Ministry of Science and Higher Education within the State assignment FSRC «Crystallography and Photonics» RAS (agreement No. 007-ГЗ/Ч3363/26) with regard to the determination method of tissue thermal damage area.

Chloroform infiltrate temperature sensor using asymmetric circular dual-core photonic crystal fiber

Md. Mahbub Hossain[1*], Rajib Mandal[1], Md. Ziaul Amin[1,2], Himadri Shekhar Mondal[1], and Md. Ekhlasur Rahaman[1]

[1] Electronics and Communication Engineering Discipline, Khulna University, Khulna 9208, Bangladesh
[2] MQ Photonics, School of Engineering, Macquarie University, New South Wales 2109, Australia

*** e-mail:** mahbub.eceku@yahoo.com

Abstract. A new temperature sensor based on asymmetry in dual circular core photonic crystal fiber (ADCPCF) is proposed where both the cores infiltrate by chloroform. To analyze the temperature dependent propagation characteristics, the thermo-optic coefficient of chloroform and silica is used. The asymmetry of the dual-core is confirmed by using the core radius of 1.615 and 1.45 μm, respectively. In the proposed design, the essential optical properties such as effective refractive index difference (birefringence), coupling length, and transmission spectra are determined by employing the finite element method (FEM) with the perfectly matched layer (PML). The effective refractive index of the chloroform varies with temperature within a certain range. Moreover, with the increase of every 1 °C temperature the effective index difference enhances to almost 4%. Also, with the reduction of every 100 nm wavelength the birefringence decrease to 0.125×10^{-3} and 0.092×10^{-3} for 35 and 30 °C temperature, respectively. The Numeric analysis shows the maximum sensitivity of 49.80 nm/°C at 1.61 mm fiber length for 2.9 μm lattice pitch with 2.25 μm air-hole diameter. Furthermore, every 1 °C temperature increment, the proposed ADCPCF exhibits approximately 16% increases of sensitivity than the existing result. In addition, the proposed ADCPCF reveals that the guiding properties like coupling length, birefringence, and transmission spectra are wavelength and temperature reliance.

Keywords: Asymmetric dual circular core photonic crystal fiber (ADCPCF); Birefringence; Chloroform; Sensitivity; Temperature Sensor.

Paper #3294 received 11 Jun 2018; revised manuscript received 11 Sep 2018; accepted for publication 14 Sep 2018; published online 30 Sep 2018. doi: 10.18287/JBPE18.04.030302.

References

1. N. Ayyanar, R. V. J. Raja, D. Vigneswaran, B. Lakshmi, M. Sumathi, and K. Porsezian, "Highly efficient compact temperature sensor using liquid infiltrated asymmetric dual elliptical core photonic crystal fiber," Optical Materials 64, 574-582 (2017).
2. J. C. Knight, "Photonic crystal fibres," Nature 424(6950), 847-851 (2003).
3. J. Broeng, D. Mogilevstev, S. E. Barkou, and A. Bjarklev, "Photonic crystal fibers: A new class of optical waveguides," Optical Fiber Technology 5(3), 305-330 (1999).
4. B. J. Eggleton, C. Kerbage, P. Westbrook, R. S. Windeler, and A. Hale, "Microstructured optical fiber devices," Optics Express 9(13), 698-713 (2001).
5. B. Shuai, L. Xia, Y. Zhang, and D. Liu, "A multi-core holey fiber based plasmonic sensor with large detection range and high linearity," Optics Express 20(6), 5974-5986 (2012).
6. T. T. Alkeskjold, J. Lægsgaard, A. Bjarklev, D. S. Hermann, J. Broeng, J. Li, and S.-T. Wu, "All-optical modulation in dye-doped nematic liquid crystal photonic bandgap fibers," Optics Express 12(24), 5857-5871 (2004).

7. Y. Lu, M. Wang, C. Hao, Z. Zhao, and J. Yao, "Temperature sensing using photonic crystal fiber filled with silver nanowires and liquid," IEEE Photonics Journal 6(3), 1-7 (2014).
8. Z. Liu, C. Wu, M.-L. V. Tse, C. Lu, and H.-Y. Tam, "Ultrahigh birefringence index-guiding photonic crystal fiber and its application for pressure and temperature discrimination," Optics Letters 38(9), 1385-1387 (2013).
9. H. Y. Choi, G. Mudhana, K. S. Park, U.-C. Paek, and B. H. Lee, "Cross-talk free and ultra-compact fiber optic sensor for simultaneous measurement of temperature and refractive index," Optics Express 18(1), 141-149 (2010).
10. J. Xie, B. Xu, Y. Li, J. Kang, C. Shen, J. Wang, Y. Jin, H. Liu, K. Ni, X. Dong, C. Zhao, and S. Jin, "High-sensitivity temperature sensor based on a droplet-like fiber circle," Applied Optics 53(18), 4085-4088 (2014).
11. Y. Yu, X. Li, X. Hong, Y. Deng, K. Song, Y. Geng, H. Wei, and W. Tong, "Some features of the photonic crystal fiber temperature sensor with liquid ethanol filling," Optics Express 18(15), 15383-15388 (2010).
12. J.-M. Hsu, C.-L. Lee, P.-J. Huang, C.-H. Hung, and P.-Y. Tai, "Temperature sensor with enhanced sensitivity based on photonic crystal fiber interferometer with material overlay," IEEE Photonics Technology Letters 24(19), 1761-1764 (2012).
13. S.-J. Qiu, Y. Chen, F. Xu, and Y.-Q. Lu, "Temperature sensor based on an isopropanol sealed photonic crystal fiber in-line interferometer with enhanced refractive index sensitivity," Optics Letters 37(5), 863-865 (2012).
14. X. Yang, Y. Lu, B. Liu, and J. Yao, "Temperature sensor based on photonic crystal fiber filled with liquid and silver nanowires," IEEE Photonics Journal 8(3), 1-9 (2016).
15. W. Qian, C.-L. Zhao, S. He, X. Dong, S. Zhang, Z. Zhang, S. Jin, J. Guo, and H. Wei, "High-sensitivity temperature sensor based on an alcohol-filled photonic crystal fiber loop mirror," Optics Letters, 36(9), 1548-1550 (2011).
16. Q. Liu, S. Li, H. Chen, Z. Fan, and J. Li, "Photonic crystal fiber temperature sensor based on coupling between liquid-core mode and defect mode," IEEE Photonics Journal 7(2), 1-9 (2015).
17. W. Lin, B. Song, Y. Miao, H. Zhang, D. Yan, B. Liu, and Y. Liu, "Liquid-filled photonic-crystalfiber-based multimodal interferometer for simultaneous measurement of temperature and force," Applied Optics, 54(6), 1309-1313 (2015).
18. K. Naeem, B. H. Kim, B. Kim, and Y. Chung, "High-sensitivity temperature sensor based on a selectively-polymer-filled two-core photonic crystal fiber in-line interferometer," IEEE Sensors Journal 15(7), 3998-4003 (2015).
19. Y. Wang, M. Yang, D. Wang, and C. Liao, "Selectively infiltrated photonic crystal fiber with ultrahigh temperature sensitivity," IEEE Photonics Technology Letters 23(20), 1520-1522 (2011).
20. Y. Cui, P. P. Shum, D. J. J. Hu, G. Wang, G. Humbert, and X.-Q. Dinh, "Temperature sensor by using selectively filled photonic crystal fiber sagnac interferometer," IEEE Photonics Journal 4(5), 1801-1808 (2012).
21. S. Kedenburg, T. Gissibl, T. Steinle, A. Steinmann, and H. Giessen, "Towards integration of a liquid-filled fiber capillary for supercontinuum generation in the 1.2-2.4 μm range," Optics Express 23(7), 8281-8289 (2015).
22. K. Nielsen, D. Noordegraaf, T. Sørensen, A. Bjarklev, and T. P. Hansen, "Selective filling of photonic crystal fibres," Journal of Optics A: Pure and Applied Optics 7(8), L13-L20, 2005.
23. C. J. de Matos, C. M. Cordeiro, E. M. Dos Santos, J. S. Ong, A. Bozolan, and C. B. Cruz, "Liquid-core, liquid-cladding photonic crystal fibers," Optics Express 15(18), 11207- 11212 (2007).
24. R. V. J. Raja, K. Senthilnathan, K. Porsezian, and K. Nakkeeran, "Efficient pulse compression using tapered photonic crystal fiber at 850 nm," IEEE Journal of Quantum Electronics 46(12), 1795-1803 (2010).
25. Q. Liu, S. Li, H. Chen, J. Li, and Z. Fan, "High-sensitivity plasmonic temperature sensor based on photonic crystal fiber coated with nanoscale gold film," Applied Physics Express 8(4), 046701 (2015).

1 Introduction

Photonic crystal fibers (PCF) have been investigated widely for their special structure and unique properties like endless single mode, tailoring zero dispersion, enhanced birefringence, and large effective mode area [1,2]. PCF is also called holey fibers (HF) or microstructure optical fibers (MOF), which has huge potential for various uses in the telecommunication data transmission devices. In addition, it has a significant impact on the traditional sensor industry. PCFs have the ability to control the light into the fiber, which was not possible earlier. They have shown extensive concentration recently due to its scope of applications in manipulating the modal properties [3]. Moreover, there are many investigators who show interest in designing highly developed sensors where the air-holes are filled with polymer, oil, gas, liquid, and liquid crystal [4-6]. These PCF based sensors have unique properties, difficulties, and design flexibility. However, it is expected that these difficulties are overcome gradually [7]. Optical temperature sensors have been shown a large amount of curiosity nowadays due to high sensitivity, linearity, and stability.

A significant attention has been given to develop efficient temperature sensor using PCF with different types of configuration. Liu et al. [8] reported an ultrahigh birefringence index-guiding PCF temperature sensor which showed 11 and 11.2 pm/°C sensitivity on behalf of the fast and slow axis, respectively. Choi et al. proposed hollow core PCF to calculate the temperature and refractive index which illustrated the sensitivity of 8.9 and 14.6 nm/°C at low and high temperature, correspondingly [9]. In 2014, Xie recommended temperature based droplet fiber which demonstrated the sensitivity of -3.102 nm/°C with reasonable cost [10]. Recently, Ayyanar reported asymmetric dual elliptical core photonic crystal fiber (DECPCF) which exhibited the sensitivity of 42.99 nm/°C [1]. The main theme of this work was to increase the sensitivity at low distance over the wide spectrum window. For this, it is measured in nm/°C. However, the fabrication complexity is increased due to the elliptical shape.

To improve the sensitivity and temperature sensing range of a sensor, unusual materials can be used to PCF fabrication like Telluride, Chalcogenide glasses, and liquid materials [11-15]. Recently, it is observed that liquid core PCFs show a large variation of refractive index depending on temperature [1]. Therefore, the development of liquid core PCFs will increase the temperature sensing ability. It is reported that PCF-based temperature sensor where the coupling is done between liquid core and defect mode has the sensitivity of 1.85 nm/°C [16]. A liquid filled PCF interferometer showed -24.757 nm/°C sensitivity for temperature range 19.5 to 22.5 °C [17]. Another report presented polymer filled dual-core PCF (DC-PCF) which has given sensitivity of 1.595 nm/°C for the temperature range of 32-38 °C [18]. In 2011 Wang proposed an ultra-sensitive temperature sensor which demonstrated light coupling involving the fundamental and rod mode and sensitivity is observed 54.3 nm/°C. Nevertheless, the delicate power of the rod mode is eliminated through fusion splicing which increased the fabrication difficulties [19]. However, these types of investigations have small temperature detecting window of 1.4 °C [16]. PCF based Sagnac interferometer presented temperature identifying window of 17 °C with low sensitivity of 2.58 nm/°C [20].

Several research groups have been reported different mechanisms for the temperature sensor to increase the sensitivity with small fiber length. In this report, to increase the sensitivity of asymmetric DCPCF (ADCPCF) sensor, adjust the two circular center core radius and either lattice pitch or air hole diameter is varied. To obtain high sensitive compact temperature sensor, the liquid, which has high-temperature sensitivity is the key requirement for the liquid filled PCF. Among the several liquids, chloroform emerges as a potential candidate for the development of liquid filled PCFs, as their refractive index is highly dependent on temperature. Moreover, chloroform is shown broad transmission window from near-infrared (NIR) to mid-infrared (MIR) regime, which can be used to detect the temperature range. In the proposed model, the optical properties like effective refractive index difference, coupling length, and transmission spectra are found by using the finite element method (FEM) through perfectly matched layer (PML).

2 Materials and Methods

2.1 Modeling of ADCPCF

In the proposed design, the dual-core circular PCF is considered where both the core is filled with chloroform. To examine the performance of temperature sensor, a circular core with asymmetric diameter is used due to increase the effective refractive index difference. As a result, it influences the coupling length and transmission spectrum when compared to symmetrical DCPCF. The transmission studies are carried out numerically for various temperature. In addition, the proposed structure is optimized by adjusting the diameter and pitch of the air-holes. Moreover, the coupling between core modes is demonstrated in the proposed design. The refractive index of chloroform is changed with temperature. Furthermore, a certain temperature range can be detected by measuring the transmission spectra and thus the accurate ambient temperature can be obtained. From the transmission spectrum, the compact temperature sensor is constructed and its sensitivity is determined. The structure parameters of proposed ADCPCF is shown in Table 1. The cross-section of the proposed ADCPCF is shown in Fig. 1. The air-holes distribution in the cladding region is a hexagonal pattern. Furthermore, 5.8 μm inter-core separation is chosen. The holes of cladding are filled up with air and the background material of cladding is made up of silica. Moreover, both of the dual-cores and air-holes are circular formed which confirm easier fabrication. However, fabrication of liquid core PCFs is already done by applying capillary forces or pressure and careful filling techniques [21-23].

Table 1 Design parameters of the proposed ADCPCF.

Pitch	2.9 μm
Air hole diameter	2.26 μm
Core-1 (radius)	1.615 μm
Core-2 (radius)	1.45 μm

2.2 Theoretical Background

For chloroform, variation of refractive index as a function of wavelength at a temperature of 20 °C can be given [24],

$$n_{20}(\lambda) = 431364 + 5632.41\times\lambda^{-2} - 2.0805\times \times 10^{8}\times\lambda^{-4} + 1.2613\times\lambda^{-6}, \quad (1)$$

where λ represents wavelength of the propagating light. Using eqs. (1), the refractive index of other temperature can be calculated by

$$n(\lambda,T) = n_{20}(\lambda) + \Delta T\frac{dn}{dT}, \quad (2)$$

where $n(\lambda,T)$ is the refractive index of chloroform at a particular wavelength λ for the desired temperature T. ΔT is the difference between the desired temperature.

Also, at 20 °C, $\frac{dn}{dT}$ gives the rate of variation of refractive index as a function of temperature and takes the value of -7.9×10^{-4} K^{-1} for chloroform [1]. The liquid chloroform has very high non-linearity and the refractive index almost equal to that of silica. The background material of the fiber is fused silica whose dispersion relationship corresponding to temperature can be written by the Sellmeier equation [25]

$$n^2(\lambda,T) = (1.31552 + 6.90754\times10^{-6}T) +$$

$$+\frac{(0.788404 + 23.5835\times10^{-6}T)\lambda^2}{\lambda^2 - (0.0110199 + 0.584758\times10^{-6}T)} +$$

$$+\frac{(0.91316 + 0.548368\times10^{-6}T)\lambda^2}{\lambda^2 - 100}.$$

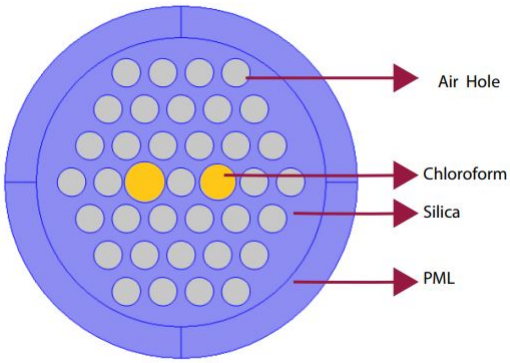

Fig. 1 Cross section of the proposed ADCPCF.

The existing forms of silica are crystalline and amorphous. If the arrangement of silica is ordered, the form is crystalline. In the amorphous form, silica is not in a specific form. Continuous heating and slow cooling is required to form crystalline silica. If the cooling is too fast, molecules of silica cannot rearrange in the role of bonds. Then the form of the silica will be amorphous. The melting temperature of silica is about 167 °C.

The coupling length of x and y-polarization can be calculated by the formula as follows [1].

$$L_C = \frac{\lambda}{2|n_{even} - n_{odd}|}. \quad (4)$$

The coupling modes inside the dual core PCF can be calculated by two even modes and two odd modes, which are also called super modes. The four basic modes n_{even}^x, n_{even}^y, n_{odd}^x, n_{odd}^y are observed in the proposed liquid filled ADCPCF. Their field distribution is shown as Fig. 2. The effective index difference between the super modes of x and y-polarization can be calculated by

$$\Delta n_{eo} = |n_{even} - n_{odd}|, \quad (5)$$

which is also called birefringence, B = Δn_{eo}. In order to find the temperature of the environment through PCF, the intensity variation of pulse propagation is calculated. According to the mode coupling theory, the optical power transfer from one core to another along the proposed ADCPCF can be calculated by [25]

$$P_{out}(\lambda) = P_{in}\exp\left(\frac{-\alpha L}{4.343}\right), \quad (6)$$

where L is the length of the proposed ADCPCF. Thus, calculating the transfer optical power in the second core with a fixed length according to output power equation when the light is injected into core of the proposed PCF. The transmittance can be given by [1]

$$T_r = 10\log_{10}\left(\frac{P_{out}}{P_{in}}\right), \quad (7)$$

where P_{in} is assumed as maximum power of P_{out}.

The sensitivity of the proposed sensor can be measured through the move of peak wavelength for changing temperature. The sensitivity can be defined as [16]

$$S = \frac{\Delta\lambda_p}{\Delta T}, \quad (8)$$

where λ_p is the peak wavelength.

3 Results and Discussion

The coupling length, transmission spectra, and sensitivity of the proposed structure are investigated by the way of calculating the effective refractive index of the coupling modes. The four basic modes n_{even}^x, n_{even}^y, n_{odd}^x, n_{odd}^y of the designed liquid filled ADCPCF are computed. The effective index difference between the super modes of x and y-polarization is calculated by Eq. (5). The variation of effective index difference of super mode with respect to wavelength for x and y-polarization from 30 to 35 °C is shown in Fig. 3. In Fig. 2, the electric field distribution of the proposed ADCPCF is presented. The arrow indicates the direction of electric field of even and odd mode for x and y-polarization.

Fig. 3 shows that when the wavelength is increased the effective refractive index difference is decreased for all temperatures. Also, with the increase of the temperature the effective refractive index difference is shown raising. The solid and dashed line indicate the effective index difference of super-modes for x and y-polarization, accordingly. This index difference is also

called birefringence which has great impact on polarization maintaining. At 1.55 µm wavelength and 30 °C temperature, the index difference Δn is 1.62×10^{-3} and 1.63×10^{-3} for x and y-polarization, respectively. At the same wavelength increasing the temperature from 30 to 35 °C, the index difference is increased to 2.02×10^{-3} and 2.03×10^{-3} for the similar polarization. Since increasing temperature presents higher index difference it influences the coupling length and transmission spectrum. Moreover, with the increase of every 1 °C temperature, the effective index difference is increased to almost 4%. Again, with the reduction of every 100 nm wavelength the index difference or birefringence is decreased to 0.125×10^{-3} and 0.092×10^{-3} for 35 and 30 °C temperature, respectively. Therefore, high temperature shows maximum index difference or birefringence. Moreover, y-polarization demonstrates more birefringence than x due to higher effective refractive index.

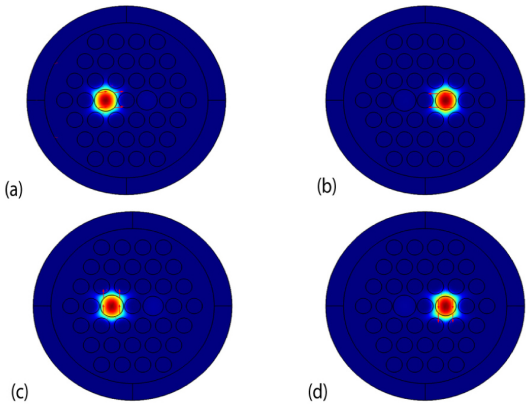

Fig. 2 Electric field distribution of proposed ADCPCF. The arrow indicates the direction of electric field of even and odd mode for x and y-polarization. (a) and (b) for x, and (c) and (d) for y-polarization.

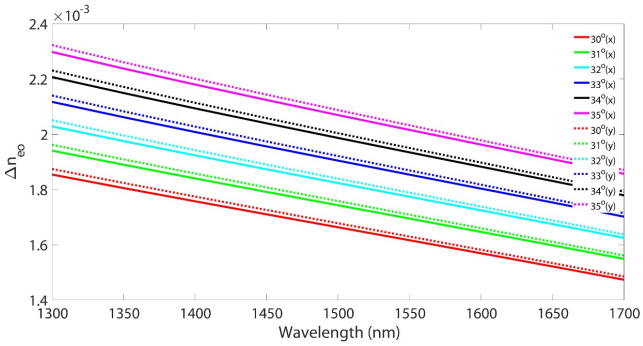

Fig. 3 Effective index difference of x and y-polarization as a function of wavelength for various temperatures. Solid and dashed line present the effective index difference of super-modes for x and y-polarization, respectively.

Coupling length illustrates the lowest value at which the light is easily transferred from one core to another one. Coupling length of ADCPCF is calculated for temperature range 30 to 35 °C. The temperature dependent coupling length as a function of wavelength for x and y-polarization are plotted in Fig. 4. Coupling length is increased from 0.35 to 0.57 mm when the wavelength is increased from 1300 to 1700 nm. Moreover, with the increase of the temperature the coupling length is decreased due to increase of the effective index difference as shown in Fig. 3. At 1.3 µm wavelength and x polarization, 0.35 mm coupling length is reduced to 0.28 mm for increasing the temperature 30 to 35 °C. The rate of this reduction is 4% for every 1 °C. However, at 1.55 µm wavelength the reduction rate is observed 4.3% for similar consideration. The related inclination is also observed for y-polarization. To propose PCF for temperature sensor, the attenuation of coupling length by temperature introduces an intense PCF sensor. Therefore, it is concluded that coupling length depends on temperature and wavelength. Also, the decrease of coupling length by asymmetric PCF arrangement will be prospective research on a powerful sensor.

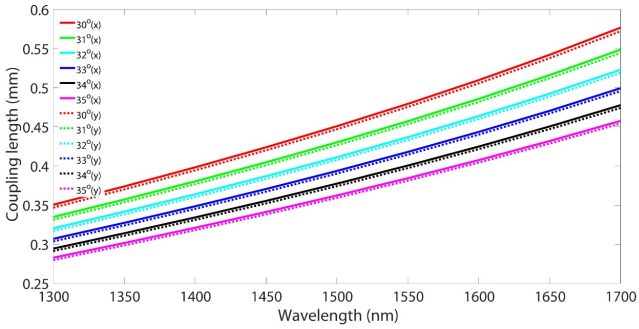

Fig. 4 Coupling length as a function of wavelength for various temperatures with asymmetric design. Solid and dashed line present the coupling length of super-modes for x and y polarization, respectively.

The transmission spectrum of the proposed ADCPCF is calculated from Eq. (7). Fiber length is important for calculating the transmission spectrum. Moreover, Longer PCFs have extra affable to temperature sense [11]. Qiang et al. used 1 mm fiber length [25]. Therefore, the length of the proposed ADCPCF fiber is taken 1.61 mm. It is observed that the dip of the transmittance of this asymmetric structure is increased when the temperature is increased. Also, it is shown that a position of six dip wavelengths for x-polarization at 1399, 1448, 1498, 1547, 1597, and 1646 nm by their consequent temperature from 30 to 35 °C. Therefore, the total wavelength shift is calculated as 249 nm in ADCPCF as shown in Fig. 5. The numeric analysis represents the dip of the wavelength transfer linearly with temperature from 30 to 35 °C, that is applied for temperature sensing purposes. However, the proposed ADCPCF shows higher wavelength shift comparing to existing report [1].

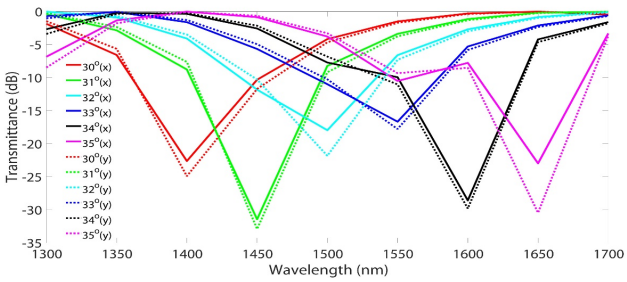

Fig. 5 Calculated transmission of asymmetric design as a function of wavelength for various temperatures. Solid and dashed line present the transmission spectrum of super-modes for x and y-polarization, respectively.

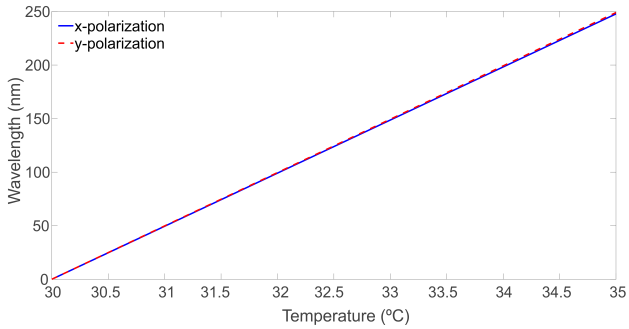

Fig. 6 Wavelength shift of the transmission spectrum for proposed ADCPCF. Temperature range is 30 to 35 °C.

Fig. 6 illustrates the calculated wavelength shift for x and y-polarization from 30 to 35 °C. For x-polarization the wavelength shift is observed 49.5 nm where y-polarization shifting is measured 49.8 nm. Moreover, Fig. 7 demonstrates the comparison of wavelength shift of the proposed ADCPCF to DECPCF [1]. The temperature range is considered from 30 to 34 °C. Result shows the maximum wavelength shift is found for y-polarization. Moreover, with the increase of temperature the wavelength shift is raised for both the models. Furthermore, the proposed ADCPCF represents wavelength shift 49.8 nm for y-polarization whereas the existing DECPCF shows 42.99 nm. Therefore, for every 1 °C temperature increment, the proposed ADCPCF represents almost 16% increasing of wavelength shift compare to DECPCF.

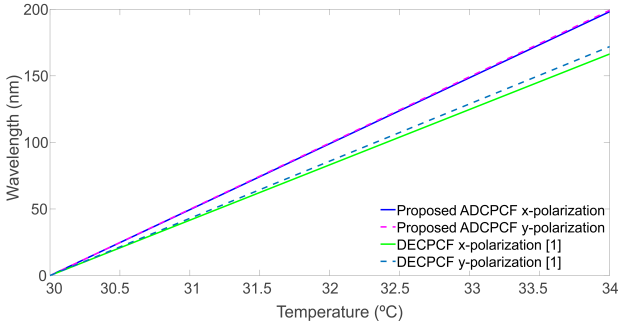

Fig. 7 Wavelength shift of the transmission spectrum for proposed ADCPCF and DECPCF [1]. Temperature range is 30 to 34 °C.

The sensitivity of the proposed sensor can be measured by the transfer of the peak wavelength for the variation of temperature. The computed wavelength transfers of the transmission spectrum for each 1 °C raising of temperature from 30 °C in the proposed ADCPCF. To achieve maximum sensitivity with a short distance, optimize the diameter and pitch of the air holes in the cladding. As the air filling factor increases by large air hole diameter and lower pitch value in the cladding, as a consequence tight confinement of light is shown into the core. So, the air-hole diameter is considered from 2 to 2.26 µm and pitch value is fixed at 2.9 µm as shown in Fig. 8. The general tendency of the figure is that increasing air hole diameter, the sensitivity is raised due to increase of the fill fraction. When air hole diameter is considered to 2 µm then sensitivity for x and y-polarization are observed 41.95 and 42 nm/°C with 1.61 mm fiber length. Moreover, the maximum sensitivity for x and y-polarization are observed 49.55 and 49.80 nm/°C at the same fiber length when this diameter is considered 2.26 µm. Therefore, for all cases sensitivity for x and y-polarization are linearly increased. However, y-polarization has shown more sensitivity than x due to the effective mode indexes, which are more efficient for y-polarization. Thus, when air-hole diameter is increased, sensitivity for y-polarization are more efficient than x-polarization. Moreover, the proposed ADCPCF shows 16% increase of sensitivity comparing to the exiting result [1].

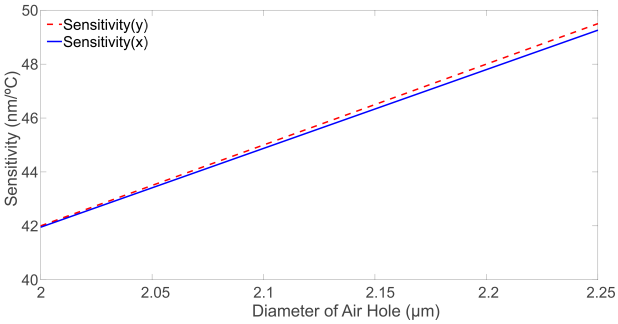

Fig. 8 Sensitivity of the proposed ADCPCF for changing air-hole diameter.

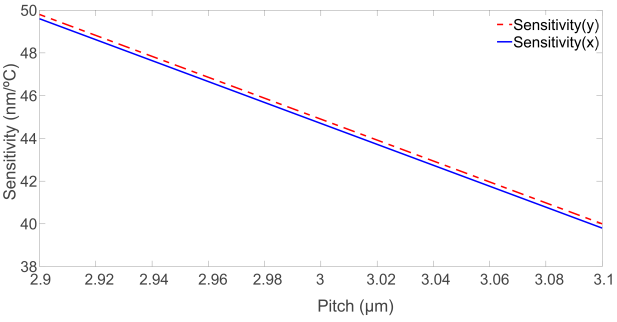

Fig. 9 Sensitivity of the proposed ADCPCF for different pitch values.

Table 2 Comparison of earlier reported PCF temperature sensors with the proposed chloroform filled ADCPCF.

PCF materials	Length (cm)	Sensitivity (nm/°C)	Reference
Selectively filled Polarization PCF (theoretical and experimental)	11.7	2.58	[20]
Alcohol filled PCF (theoretical and experimental)	6.1	6.6	[15]
Liquid and defect mode PCF (theoretical)	10	-1.85	[16]
Liquid filled PCF (theoretical and experimental	0.7	-24.75	[17]
Polymer PCF (experimental)	23	1.595	[18]
Plasmonic PCF with gold (theoretical)	0.1	-2.15	[25]
Chloroform infiltrated DECPCF (theoretical)	1.41	42.99	[1]
Chloroform filled ADCPCF (proposed)	0.161	49.80	

In order to optimize the pitch value, the value is increased from 2.9 to 3.1 µm with 0.1 µm step size while air-hole diameter is fixed at 2.26 µm as shown in Figure. 9. When pitch value is considered to 2.9 µm then sensitivity for x and y-polarization are shown 49.60 and 49.80 nm/°C with 1.61 mm fiber length. Increasing the pitch value to 3.1 µm then sensitivity of x and y-polarization are reduced to 39.80 and 40 nm/°C, respectively. Noted that with the increase of the pitch value, sensitivity is decreased for both x and y-polarization. This is due to the propagation modes, which are not effective by increasing the air-hoes distance. As a result, light scattering is increased in the fiber. Thus, the proposed PCF structure is a novel compact temperature sensor depend on asymmetric circular core diameter with sensitivity of 49.80 nm/°C at 1.61 mm, which is much higher than any temperature-based asymmetric ADCPCF sensor. In Table 2, the comparison is shown of different temperature sensor based on PCF to the proposed ADCPCF model. Nevertheless, the negative sensitivity value demonstrates the symmetric arrangement of PCFs.

4 Conclusion

In this report, a high sensitive compact temperature sensor using liquid filled PCF is proposed. Chloroform, which is a temperature-sensitive liquid is inserted into the dual circular core of the proposed ADCPCF. Typically, the asymmetric procedure is illustrated by suitably changing the radius in one of the cores of ADCPCF to enhance the sensitivity. The thermo-optic coefficient of chloroform and silica is utilized to calculate the temperature sensitivity. Moreover, the sensitivity of temperature in the proposed ADCPCF is analyzed through calculation of coupling length and transmission spectrum. In addition, the highest sensitivity is achieved by optimizing the diameter and lattice pitch of the air-holes. The proposed novel temperature sensor based on asymmetric circular diameter shows the high sensitivity of 49.80 nm/°C at 1.61 mm fiber length. This is the highest sensitivity using ADCPCF based temperature sensor. Furthermore, the proposed temperature sensor illustrates the guiding properties is temperature and wavelength dependence. The most important benefit of the proposed PCF based temperature sensor is simple to fabricate by applying the current fabrication procedures.

Disclosures

All authors declare that there is no conflict of interests in this paper.

Interaction of erythrocytes in the process of pair aggregation in blood samples from patients with arterial hypertension and healthy donors: measurements with laser tweezers

Petr B. Ermolinskiy[1*], Andrei E. Lugovtsov[1,2], Anastasiya I. Maslyanitsina[1], Alexey N. Semenov[1,2], Larisa I. Dyachuk[3], and Alexander V. Priezzhev[1,2]

[1] Department of Physics,
[2] International Laser Center, and
[3] Medical Research and Education Center of M.V. Lomonosov Moscow State University, Moscow, Russia.

*** e-mail:** peter.ermolinskiy@biomedphotonics.ru

Abstract. Two-channel laser tweezers are used to measure the interaction kinetics of two erythrocytes at the initial stage of aggregation, i.e., the formation of a pair aggregate in vitro. The study of erythrocytes interaction is important both for understanding the fundamental aggregation mechanisms and for evaluating the differences in kinetics and dynamics of aggregation, depending on the presence or absence of diseases that disturb the blood flow parameters and, therefore, the oxygen supply to tissues. We analyse the kinetics and dynamics of pair aggregation of erythrocytes in blood samples from more than 60 patients with arterial hypertension, as well as from a group of healthy donors. The results show that both kinetics and dynamics of erythrocyte aggregation are changed in the presence of the considered pathology. © 2018 Journal of Biomedical Photonics & Engineering.

Keywords: aggregation; arterial hypertension; optical trap; manipulation of single cells; aggregation force; erythrocytes.

Paper #3298 received 31 Aug 2018; revised manuscript received 16 Sep 2018; accepted for publication 19 Sep 2018; published online 30 Sep 2018. doi: 10.18287/JBPE18.04.030303.

References

1. A. Ashkin, J. M. Dziedzic, J. E. Bjorkholm, and S. Chu, "Observation of a single-beam gradient force optical trap for dielectric particles," Optics Letters 11(5), 288-290 (1986).
2. A. Ashkin, J. Dziedzic, "Optical trapping and manipulation of single living cells using infra-red laser beams," Berichte der Bunsen-Gesellschaft für Physikalische Chemie 98, 254-260 (1989).
3. A. Ashkin, Optical Trapping and Manipulation of Neutral Particles Using Lasers: a reprint volume with commentaries, World Scientific Publishing Co. Pte. Ltd., Singapore (2006).
4. K. Lee, A. V. Danilina, M. Kinnunen, A. V. Priezzhev, and I. Meglinski, "Probing the red blood cells aggregating force with optical tweezers," IEEE Journal on Selected Topics in Quantum Electronics 22(3), 7000106 (2016).
5. D. S. Moura, D. C. N. Silva, A. J. Williams, M. A. C. Bezerra, A. Fontes, and R. E. de Araujo, "Automatic real time evaluation of red blood cell elasticity by optical tweezers," Review of Scientific Instruments 86(5), 053702 (2015).
6. L. Yu, Y. He, A. Chiou, and Y. Sheng, "Deformation of biconcave Red Blood Cell in the Dual-beam Optical Tweezers," Proceedings of the 2011 COMSOL Conference, Boston (2011).
7. H. M. Nussenzveig, "Cell membrane biophysics with optical tweezers," European Biophysics Journal 47(5), 499-514 (2018).

8. A. V. Korobtsov, S. Kotova, N. Losevsky, A. Mayorova, V. Patlan, E. Timchenko, N. Lysov, and E. Zarubina, "Optical tweezers technique for the study of red blood cells deformation ability," Laser Physics 22(7), 1265-1270 (2012).
9. S. Hu, D. Sun, "Automated transportation of single cells using robot-tweezer manipulation system," Journal of Laboratory Automation 16(4), 263-270 (2011).
10. T. Sugiura, S. Maeda, and A. Honda, "Pulse laser assisted optical tweezers for biomedical applications," 2012 Annual International Conference of the IEEE Engineering in Medicine and Biology Society, San Diego, CA, 4479-4481 (2012).
11. A. Y. Maklygin, A. V. Priezzhev, A. Karmenian, S. Y. Nikitin, I. S. Obolenskii, A. E. Lugovtsov, and K. Li, "Measurement of interaction forces between red blood cells in aggregates by optical tweezers," Quantum Electronics 42(6), 500–504 (2012).
12. V. V. Tuchin, "Fundamentals of laser biomedicine," Chap. 1 in Lasers and fiber optics in biomedical research, V.V. Tuchin (Ed.), 2nd edition, Fizmatlit, Moscow, 10-66 (2010) [in Russian].
13. A. V. Priezzhev, K. Lee, N. N. Firsov, and J. Lademann, "Optical Study of RBC Aggregation in Whole Blood Samples and Single Cells," Chap. 1 in Handbook on Optical Biomedical Diagnostics, V. V. Tuchin (Ed.), 2nd Edition, SPIE Press Bellingham, WA, United States (2016).
14. O. Baskurt, B. Neu, and H. Meiselman, Red Blood Cell Aggregation, CRC Press, Boca Raton, United States (2012).
15. S. Chien, L. A. Sung, S. Simchon, M. M. L. Lee, K.-m. Jan, and R. Skalak, "Energy balance in red cell interactions," Annals of the New York Academy of Sciences 416(1), 191-206 (1983).
16. K. Lee, C. Wagner, and A. V. Priezzhev, "Assessment of the "crossbridge"-induced interaction of red blood cells by optical trapping combined with microfluidics," Journal of Biomedical Optics 22(9), 091516 (2017)
17. K. Lee, A. Danilina, A. Potkin, M. Kinnunen, A. Priezzhev, and I. Meglinski, "RBC aggregation dynamics in autologous plasma and serum studied with two-channel optical tweezers," Proceedings of SPIE 9917, 991704 (2016).
18. K. Lee, A. Muravyov, A. Semenov, C. Wagner, A. Priezzhev, E. Lyubin, and A. Fedyanin, "Gamma globulins-induced interaction between two red blood cells: forces measurement with optical tweezers," Proceedings of SPIE 10336, 1033606 (2017).
19. J. Tripette, T. Alexy, M.-D. Hardy-Dessources, D. Mougenel, E. Beltan, T. Chalabi, R. Chout, M. Etienne-Julan, O. Hue, H. J. Meiselman, and P. Connes, "Red blood cell aggregation, aggregate strength and oxygen transport potential of blood are abnormal in both homozygous sickle cell anemia and sickle-hemoglobin C disease," Haematologica 94(8), 1060-1065 (2009).
20. O. Baskurt, H. Meiselman, "Erythrocyte aggregation: basic aspects and clinical importance," Clinical Heomohreology and Microcirculation 53(1-2), 23-37 (2013).
21. E. Konstantinova, L. Ivanova, T. Tolstaya, and E. Mironova, "Rheological properties of blood and parameters of platelets aggregation in arterial hypertension," Clinical Hemorheology and Microcirculation 35(1-2), 135-138 (2006).
22. M. D. Khokhlova, E. V. Lyubin, A. G. Zhdanov, A. A. Fedyanin, S. Y. Rykova, and I. A. Sokolova, "Normal and system lupus erythematosus red blood cell interactions studied by double trap optical tweezers: direct measurements of aggregation forces," Journal of Biomedical Optics 17(2), 025001 (2012).
23. G. Cicco, A. Pirrelli, "Red blood cell (RBC) deformability, RBC aggregability and tissue oxygenation in hypertension," Clinical Hemorheology and Microcirculation 21(3-4), 169-177 (1999).
24. B. Sandhagen, "Red cell fluidity in hypertension," Clinical Hemorheology and Microcirculation 21(3-4), 179-181 (1999).
25. P. Gyawali, R. S. Richards, D. L. Hughes, and P. Tinley, "Erythrocyte aggregation and metabolic syndrome," Clinical Hemorheology and Microcirculation 57(1), 73-83 (2014).
26. P. Gyawali, R. S. Richards, and E. U. Nwose, "Erythrocyte morphology in metabolic syndrome," Expert Review of Hematology 5(5), 523-531 (2012).
27. E. Pytel, P. Duchnowicz, P. Jackowska, K. Wojdan, M. Koter-Michalak, and M. Broncel, "Disorders of erythrocyte structure and function in hypertensive patients," Medical Science Monitor 18(8), 331-336 (2012).
28. M. Kaczmarska, M. Fornal, F. H. Messerli, J. Korecki, T. Grodzicki, and K. Burda, "Erythrocyte membrane properties in patients with essential hypertension," Cell Biochemistry and Biophysics 67(3), 1089-1102 (2013).
29. J. Badlam, T. Bull, "Steps forward in the treatment of pulmonary arterial hypertension: latest developments and clinical opportunities," Therapeutic Advances in Chronic Disease 8(2-3), 47–64 (2017).
30. T. Nieminen, G. Knöner, N. R. Heckenberg, and H. Rubinsztein-Dunlop, "Physics of optical tweezers," Methods in Cell Biology 82, 207-36 (2007).
31. A. Gennerich, Optical Tweezers. Methods and Protocols, Humana Press (2017).
32. Video demonstrations of experiments with laser tweezers, obtained by P.B. Ermolinskiy, A.E. Lugovtsov, A.I. Maslyanitsina, A.N. Semenov, L.I. Dyachuk, A.V. Priezzhev.

33. J. Lasch, G. Küllertz, and J. R. Opalka, "Separation of erythrocytes into age-related fractions by density or size? Counterflow centrifugation," Clinical Chemistry and Laboratory Medicine 38(7), 629-632 (2000).
34. M. Tavakol, O. Abouali, M. Yaghoubi, and G. Ahmadi, "Dispersion and Deposition of Ellipsoidal Particles in a Fully Developed Laminar Pipe Flow Using Non-Creeping Formulations for Hydrodynamic Forces and Torques," International Journal of Multiphase Flow 75, 54-67 (2015).
35. R. J. Fish, M. Neerman-Arbez, "Fibrinogen gene regulation," Thrombosis and Haemostasis 108(3), 419-26 (2012).
36. A. N. Semenov, A. E. Lugovtsov, K. W. Li, A. A. Fabrichnova, Y. A. Kovaleva and A.V. Priezzhev, "Applying methods of diffuse light scattering and optical trapping for assessing blood rheological parameters: erythrocytes aggregation in diabetes mellitus," Izvestie Saratov University (N.S.) 17(2), 85–97 (2017) [in Russian].

1 Introduction

Laser tweezers (LT) are devices that allow for trapping and manipulation of microobjects without direct mechanical contact with them. The principle of their operation is based on the interaction of a sharply focused laser beam with the trapped microobject. For the first time the possibility of trapping and manipulation of dielectric particles by means of a sharply focused laser beam was demonstrated by Arthur Ashkin in 70s of the last century by the example of spherical microparticles in water, which finally led to the invention of LT [1]. They became a necessary tool in the solution of many problems of physics and biology [2, 3]. For example, LT are used for living cells trapping and manipulation, sorting, measuring the cell elasticity and deformability [4, 5, 6, 7, 8]. LT are also used to study the cells cytoskeletons, to measure viscosity and elasticity of biopolymers [3]. It is also possible to measure the forces of interaction between living cells, in particular, the red blood cells [4]. The field of LT applications is permanently expanding.

To date different schemes of LT have been designed, aimed at solving different research and technical problems. For example, there are setups that allow automated trapping and manipulation of single cells [9]. Alongside with continuous-wave lasers, pulsed lasers are also applied in LT schemes in order to improve the trapping efficiency and manipulating velocity [10]. Using a circularly polarised trapping beam, one can rotate the trapped cell [3]. The character of trapping depends on the beam profile [3]. In our experiments we used two-channel laser tweezers based on the continuous-wave lasers with Gaussian beam profile to measure the kinetic and dynamic parameters of erythrocytes interaction in the process of pair aggregation (see Materials and methods).

When the laser beam traps a living cell, it is important to monitor the influence of the optical trapping on the cell properties, since the capture can affect the linear dimensions, shape and orientation of the cell depending on the elasticity of its membrane and the trapping force [11]. The laser radiation wavelength should be chosen in the range of maximum optical transparency of the studied object, thus eliminating the thermal effect, i.e., the object heating in the process of investigation [12].

The interaction of erythrocytes with each other leading to the formation of aggregates is one of the most important mechanisms regulating the fluidity of blood in vessels. This interaction is referred to as aggregation, and it essentially affects the blood microcirculation and rheology of blood in the entire organism [13]. In the vessels *in vivo* the aggregation of erythrocytes is a spontaneous and reversible process, since under the effect of shear stresses that arise in the blood flow the aggregates are separated into individual cells, which can aggregate again as a result of subsequent interaction. To this day the erythrocytes aggregation mechanism has not been fully studied [14]. The interaction of aggregating erythrocytes is commonly described using two models differing in the definition of forces responsible for aggregate formation. In the model of depletion layer the interaction is described by osmotic forces that arise in the solutions of macromolecules surrounding the cells, e.g., in blood plasma [14]. In the model of bridges, the interaction is described by the forces that arise due to adsorption of macromolecules at the surface of membranes of adjacent erythrocytes [15]. To date there are serious arguments in favour of both models [14, 16]. However, making a final decision on the correctness of model considerations requires additional studies.

The processes of aggregation and disaggregation of erythrocytes can be described by a set of parameters, the meaning of which depends on the method of measurement, in particular, on whether the parameters are measured in a sample of large ensemble of cells, e.g., in whole blood, or in a sample of single erythrocytes (highly diluted suspension of single cells). The values of these parameters depend on the composition of the medium surrounding the erythrocytes. In the organism (in vivo) it is the blood plasma, but out of the organism (in vitro) the composition of the environment can be purposely changed for the sake of study. In particular, the measurements are performed in blood serum (purified plasma free of fibrinogen protein, which is one of the main proaggregants) [17] or in solutions of

macromolecules affecting the processes of blood cells interaction in a certain way [18].

When such parameters of aggregation as the aggregation rate and the hydrodynamic strength of aggregates differ from the normal values to higher values, the viscosity of blood increases that decelerates the blood flow and disturbs microcirculation in the organism. The abnormal aggregation of erythrocytes was observed by a number of researchers under the diabetes mellitus, arterial hypertension, cardiovascular pathologies, cerebrovascular insufficiency [19, 20, 21]. In Ref. [22] the alterations of such aggregation parameters of erythrocytes as the interaction force and the aggregation rate from the norm in patients with systemic lupus erythematosus were reported. Most researchers performed measurements of microrheological parameters of erythrocytes (i.e., the parameters of cell aggregation and deformability) with samples of whole blood, i.e., large ensembles of particles, using the methods of ectacytometry and diffuse light scattering [13]. In the present study, the changes of cell aggregation parameters (aggregation time and interaction forces) were investigated for pairs of single blood cells from patients with arterial hypertension. In the study of interaction between single erythrocytes, the introduced aggregation parameters are different from those in a large cell ensemble, since in the latter case the measured values are averaged over all cells in the ensemble.

Arterial hypertension (AH) is a chronic disease characterized by persistently high arterial pressure. Under this disease the microrheological properties of blood become changed, which essentially affects the blood flow in the vessels [23, 24, 25]. Usually, the patients with AH suffer from concomitant diseases, e.g., in the case of metabolic syndrome [26]. To date the results are obtained that evidence in favour of the presence of oxidative balance disturbance in erythrocytes of patients with AH [27], which may cause hypoxemia and, in turn, further increase of the arterial pressure [28]. At the present new methods of AH treatment by correcting the aggregation state of erythrocytes are being developed [29]. Naturally, in this case the methods are required capable of quantitative assessment and monitoring of this state not only at the level of an ensemble of cells, but also at the level of interaction of individual erythrocytes. Thus, by studying the process of red blood cells aggregation, its origin and the factors that affect it, we approach the understanding of the aggregation mechanism, which in the future may give rise to novel methods of treatment of AH and other socially significant diseases.

The aim of the present work is to study the kinetics and dynamics of interaction of pair-aggregating erythrocytes using the laser tweezers in the blood samples from a group of patients with AH and a control group of healthy donors. The obtained data are statistically analysed and systemised; the values of the measured parameters for the two groups are compared.

2 Experimental setup

In this work, we used the two-channel homemade laser tweezers. A schematic layout of the setup is presented in Fig. 1. The basic elements are two diode-pumped Nd:YAG lasers (Shanghai Dream Lasers Technology) with the wavelength 1064 nm and the output power 200 mW, and the water-immersion objective OLYMPUS with high numerical aperture (NA = 1.00). The wavelength of the lasers is in the range of optical transparency of haemoglobin, which is the main component of an erythrocyte [12]. This fact allows elimination of heating effect of the trapping beam on the blood cells, located under the cover glass in a cuvette filled with saline solution. The power of the beams varied within the range 20-30 mW. Earlier we have shown [11] that in such cuvette the temperature of a cell increases by $\sim$1 ^{o}C per each 10 mW of laser radiation power during the trapping time about 5-10 minutes. Therefore, in our experiments the temperature of cells could differ from that of the environment by less than 3 ^{o}C, which lies within the limits of physiologic variations. Since the experiment with a pair of erythrocytes takes the time of 1-2 minutes, such thermal effect does not lead to essential changes of the studied parameters. The video images of interacting erythrocytes during every measurement were recorded using the CMOS camera DCC1645C (Thorlabs).

In the setup, two laser beams allow trapping and manipulation of two initially not interacting blood cells, drawing them together until point contact, overlapping their membranes. Typically, one of the beams is immobile and possesses greater trapping force than the other mobile one, whose position is varied by means of a controlled mirror. This facilitates a fixed position of erythrocyte in the immobile trap and direct measurement of interaction forces between the erythrocytes by means of moving the mobile beam. For example, in the case of membrane contact of the trapped erythrocytes under the gradual decrease of the beam powers and, therefore, trapping forces, at a certain moment of time the aggregation of the erythrocytes will occur, and the aggregated erythrocyte will move to the immobile beam trap region. Using a beam expander in this setup allows increasing the trapping gradient force, since by increasing the beam aperture we increase the convergence angle of the laser beam in the focal point of the objective, which increases the intensity gradient in the beam waist region [30]. In the setup, the power of each trap was variable by means of two polarisers, which, in turn, allowed controlling the trapping force. The physical principle of optical trapping formation and the basic components of laser tweezers are described in more detail in Ref. [31].

3 Materials and methods of measurements

The Medical Research and Education Centre of M.V. Lomonosov Moscow State University provided the blood samples used in our work after getting the informed consent of each patient. All experiments were

performed during 5 hours from the moment of blood sampling. The sample used for measurements with LT was a suspension of erythrocytes, diluted by the autologous erythrocyte-depleted plasma, which was obtained as follows. The patient's whole blood samples were centrifuged (Eppendorf MiniSpin, Germany) at 180×g for 10 minutes. The sediment erythrocytes were extracted from the plasma with micropipette, and the rest of the plasma was centrifuged at 3000×g during 10 minutes for sedimentation of thrombocytes. After the separation of plasma from the sediment thrombocytes, the erythrocytes were diluted in the thrombocyte-free plasma at a ratio 1:1000. Such dilution is needed because in the study of single cells interaction the distance separating the adjacent non-interacting cells should be large enough not to affect the measurement process. The prepared sample was placed in the cuvette formed by the object glass slide and the cover one, the spacing between them being of the order of 100 μm (Fig. 2).

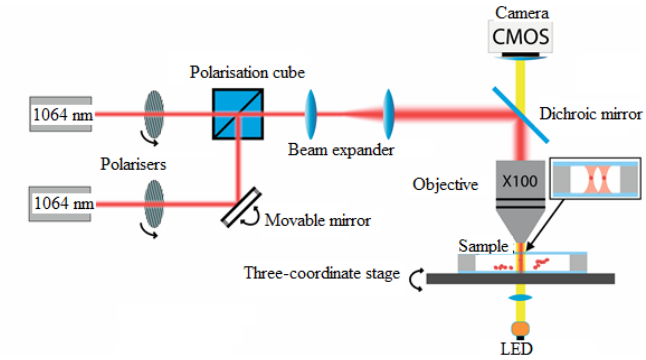

Fig. 1 Schematic diagram of the two-channel laser tweezers.

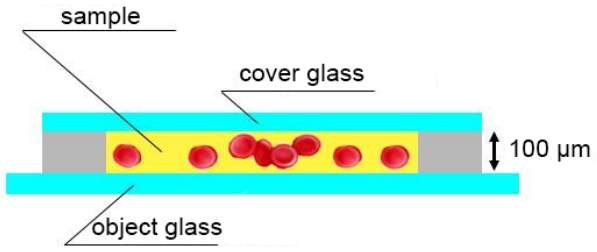

Fig. 2 Schematic diagram of blood sample cuvette.

After placing the cuvette with erythrocytes under the objective, objective focusing, and searching for two initially non-interacting erythrocytes they were sequentially captured by two traps, brought together till the contact by moving the mobile trap, and subjected to measurements. Three parameters were measured in the experiments, namely, the erythrocytes aggregation time (i.e., the time of their stacking upon each other resulting in the formation of a pair aggregate), the aggregation force (AF) and the disaggregation force (DF) (Fig. 3). The video demonstrations of the measurement of these parameters are available at [32].

The time of erythrocyte aggregation is the time interval from the contact of their membranes to the formation of a pair aggregate. Two erythrocytes are brought together until the state of a "point contact", i.e., the minimal overlap allowed by the setup [32]. Then the laser beams that form the traps are shut off and the spontaneous aggregation of erythrocytes by stacking of the cells upon each other is observed.

The aggregation force is the minimal force of optical trapping necessary to prevent spontaneous aggregation of two interacting cells. In this case, the surfaces of two erythrocytes are brought to overlapping using the LT by nearly 40%, which is controlled visually. We choose the degree of overlapping phenomenologically as the most suitable for performing the experiments. Then the trapping force of one of the traps is gradually reduced until this force can prevent the beginning of the spontaneous aggregation of the cells.

The disaggregation force is the minimal force required to separate the pair of aggregated erythrocytes. In this case two interacting erythrocytes overlap by nearly 40% of their surface (which is controlled visually), and the mobile trap is displaced trying to separate the cells. If the separation is successful, the two erythrocytes are returned to the initial position (40% overlap of membranes), the trapping force is slightly reduced, and the preceding steps are repeated until the force is unable to prevent the spontaneous aggregation of two cells. We chose the initial degree of overlap of the cells for measuring the disaggregation force phenomenologically as the most suitable for performing the experiments.

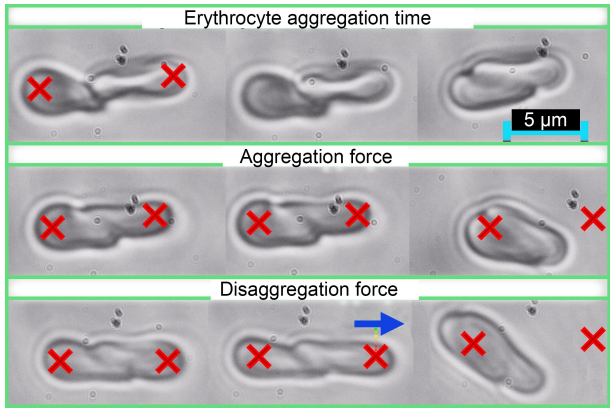

Fig. 3 Photo illustration of the processes of measuring the aggregation time, aggregation force, and disaggregation force of erythrocytes. Red crosses denote the positions where the cells were optically trapped.

The erythrocytes of human blood are different in age, size, and aggregation properties [33]. Therefore, for each blood sample the results were averaged, namely, the aggregation time was measured in 10 pairs of cells, and the AF and DF were measured in 5 pairs. All results were statistically analysed using the Statistica 13 software, and the data of donors from the control group and the patients with AH were compared using the standard Student's t-test for independent data samples.

The typical statistical spread of values in the measurements of AF and DF for one patient due to the difference of cells did not exceed 10%.

For measuring the dynamical characteristics of interaction of single cells, namely, the forces, the laser tweezers were calibrated by comparing the optical trapping force at a definite power of the laser beam with the viscous friction force (Stokes drag), acting on a trapped erythrocyte in a flow (Fig. 4). For this purpose, the erythrocyte was trapped in one channel of the laser tweezers and a flow of solvent solution was created with respect to it by moving the object stage with the cuvette. In the process of gradual increase of the flow velocity, a moment comes when the trapping force becomes smaller than the force of viscous friction, and the erythrocyte affected by the latter is released from the trap. Under the effect of the viscous friction force, the erythrocyte is deformed (elongated) becoming spheroid-like. Therefore, for the calculation of this force we modelled the erythrocyte by a spheroid, the form factor for which is presented in Ref. [34]. The video demonstration of the laser tweezers calibration is available at [32]. Thus, we obtain the experimental dependence of the viscous friction force upon the power of the laser beam. In this consideration, the viscous friction force coincides with the trapping force, since these forces are balanced when the erythrocyte is released from the trap. An example of the calibration curve is presented in Fig. 5.

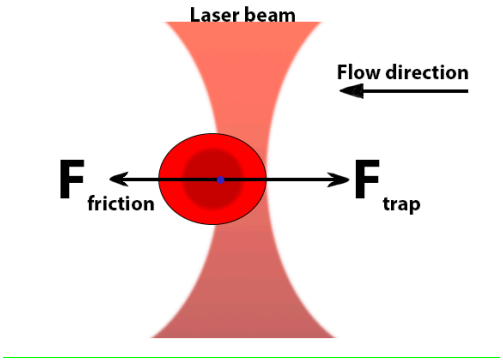

Fig. 4 Schematic comment to the process of laser tweezers calibration.

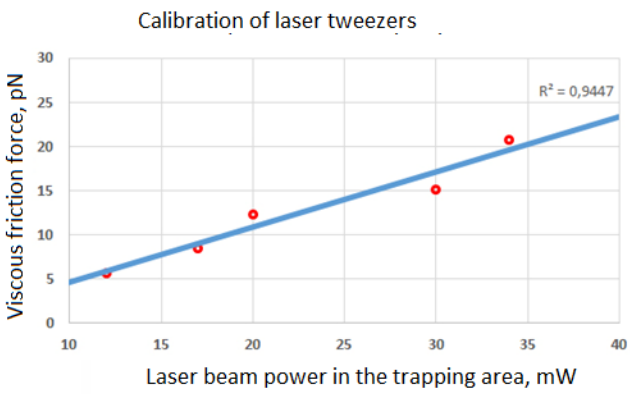

Fig. 5 Calibration curve for the laser tweezers.

4 Results and discussion

The erythrocyte aggregation parameters were measured in blood samples of 67 patients with AH aged 62 ± 12 and 8 donors of the control group (without AH and any other chronic diseases) aged 57 ± 9. The results are presented in Fig. 6. One can conclude that in the blood of patients the erythrocytes aggregate faster than in the blood of donors from the control group. In the case of AH the aggregation time is smaller by the statistically significant value of 24 ± 3%. In other words, during the same time more aggregates are produced in the blood of the patients with AH, which leads to the increased viscosity of blood and, therefore, to the disturbance of blood microcirculation. No statistically significant difference in the erythrocyte aggregation force measured in the blood of patients with AH and healthy donors of the control group was detected, whereas the disaggregation force is by 28 ± 5% greater in the patients with AH than in the donors of the control group, which is a statistically significant difference ($p < 0.05$). Therefore, in people suffering from AH the dispersion of erythrocytes requires higher shear stresses, than in healthy people.

The content of blood proteins in the patients with AH is presented in Table 1.

Table 1 Results of blood biochemical analysis in patients with AH in comparison with the norm limits. The norm limits are adopted from Refs. [35].

	AH	Norm
Fibrinogen, g/l	3.8 ± 0.5	From 1.5 to 3.5
Total protein, g/l	70 ± 4	From 60 to 83
Albumin, g/l	43 ± 2	From 38 to 50

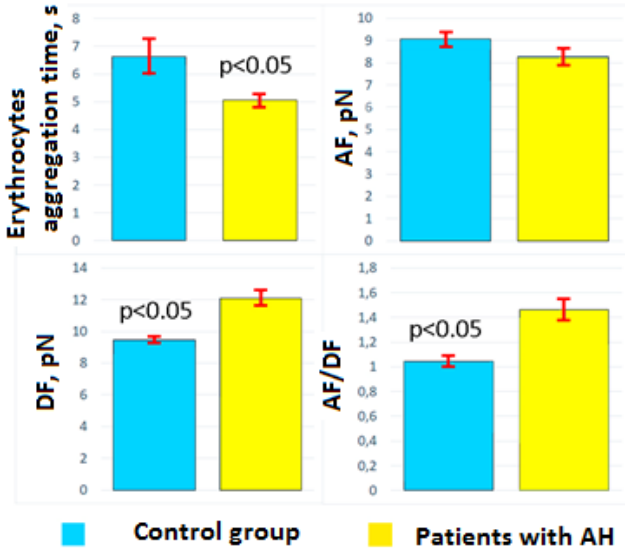

Fig. 6 Aggregation parameters: erythrocytes aggregation time, AF, DF and AF/DF for the patients with AH and the control group. The vertical bars show the mean-root-square error of mean values.

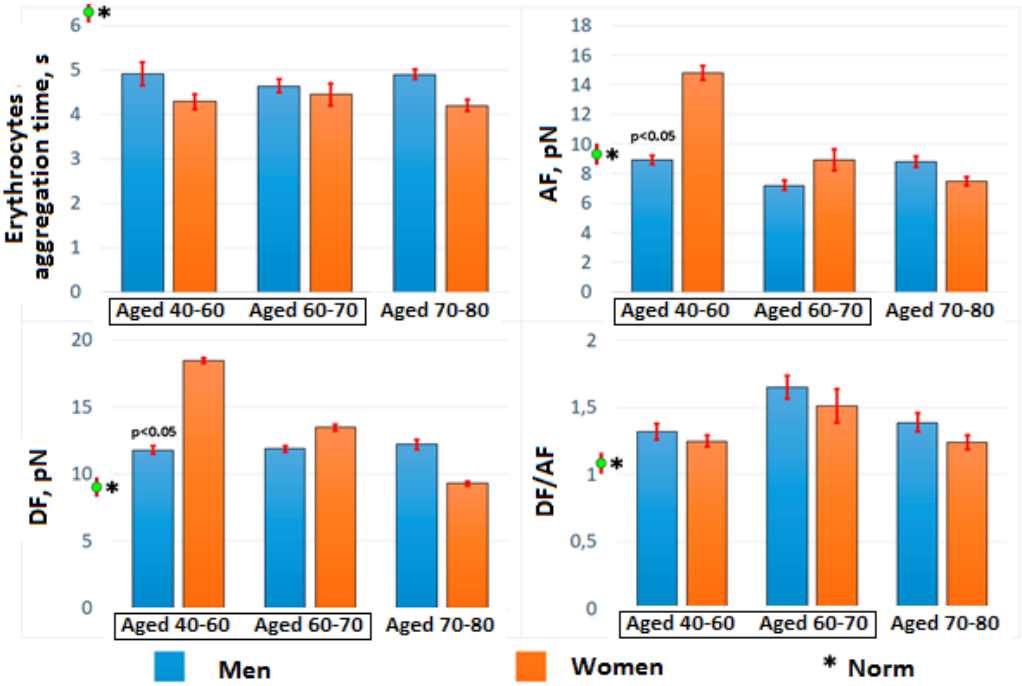

Fig. 7 Aggregation parameters: the erythrocytes aggregation time, AF, DF and the ratio DF/AF in men and women with AH for three age groups. Vertical bars indicate the mean-root-square error of mean values.

In patients with AH the concentration of fibrinogen typically corresponds to the upper limit of the norm (Table 1). Since the fibrinogen macromolecules are proaggregants, the enhanced aggregation of cells due to the increased concentration of this protein in the blood plasma of people with AH is expected.

The exact values of AF and DF can be different for the erythrocytes of different persons. However, our data show that the ratio of DF to AF can be more informative and stable than the parameters of the forces considered separately [36]. Thus, according to our data in the case of AH the DF/AF ratio amounts to nearly 1.5, while for the control group it is about 1.0. In future, the DF/AF ratio may become a new diagnostic indicator of pathology.

Fig. 7 presents the distributions of aggregation parameters for male and female patients with AH aged in ranges of 40-60, 60-70 and 70-80. Since in the latter group due to the age the patients could suffer from concomitant diseases and purely age-related changes, in our case this group carries less reliable information. For healthy donors the values of the measured parameters are shown at the ordinate axis (with green point), because due to the smallness of the sample (N = 8) their age distribution appears to be not correct. In the first two age groups, the aggregation time difference between male and female is statistically small. AF and DF in this sample monotonically decrease with age in women and demonstrates statistically significant difference from the same parameters in men. Within one age group the DF/AF ratio remains almost unchanged, however, between the age groups it differs with statistical significance ($p < 0.05$).

5 Conclusions

The results of the measurements of erythrocyte aggregation parameters performed by means of laser tweezers according to the protocols developed by us have shown that such parameters as the cell aggregation time, disaggregation force, aggregation force, and the ratio of disaggregation to aggregation force in patients with arterial hypertension (AH) differ from those in the persons from the control group. The difference of aggregation parameters between two groups may be due to the pathological changes of both the properties of erythrocytes themselves, their morphology, and the composition of plasma in which they are suspended. Except fibrinogen, one of the main proaggregants, the concentration of which in patients with AH is somewhat above the range of norm, the protein composition of plasm of the majority of patients with AH does not leave the limits of norm. This may be an evidence of the dominating effect of the properties inherent in erythrocytes themselves (mechanical properties of the membrane and viscosity of cytosol) on the aggregation parameters of erythrocytes.

In men and women with arterial hypertension within one age group, the aggregation force and the disaggregation force statistically differ, while the disaggregation to aggregation force ratio remains within the error limits. Further acquisition of statistical data is expected to show whether the disaggregation to aggregation force ratio can be a reliable indicator of blood condition in patients with arterial hypertension.

Disclosures

The authors have no relevant financial interests in this article and no potential conflicts of interest to disclose.

Acknowledgments

The authors are grateful to Dr. Kisung Lee for fruitful discussions during the experiments and preparing the paper.

The work was carried out under the financial support from the Russian Scientific Foundation (grant No. 18-15-00422).